Performance of large diameter steel tubes from a floating offshore wind turbine under lateral impact loads

Yongli Ren[a], Zhaolong Yu[b,c], Xugang Hua[a], Jørgen Amdahl[b,c], Zhengqing Chen[a]

[a] *Key Laboratory for Bridge and Wind Engineering of Hunan Province, College of Civil Engineering, Hunan University, Changsha, Hunan, China*

[b] *Department of Marine Technology, Norwegian University of Science and Technology, Norway*

[c] *Centre for Autonomous Marine Operations and Systems, Norwegian University of Science and Technology, Norway*

ABSTRACT: Floating offshore wind turbines (FOWTs) are expected to be increasingly installed in the world to harvest wind power in deep waters. Offshore wind turbines are often located near the coasts close to the traffic lanes and are exposed to safety threats from collisions by passing and visiting ships. It is therefore of great importance to investigate the impact mechanics in ship-FOWT collisions and propose practical design methods to protect from the collision loads. This paper presents a series of experimental and numerical studies on the performance of steel tubes from a NREL 5 MW spar-type FOWT under lateral impact loads. The experiments are designed and conducted at a scale of 1:30, where a rigid indenter mounted on a pendulum system is accelerated to collide into the scaled tubes. Global motions of the impacted tubes are accounted for an equivalent single-degree-of-freedom (SDOF) model for the rigid FOWT motions. Finite element (FE) models were established in LS-DYNA software. The effects of impact velocity as a crucial factor on the performance of the tubes against impact loads were discussed. Existing theoretical solutions for the lateral indentation resistance of the tubes were compared to the experimental and numerical results.

1 INTRODUCTION

Floating offshore wind turbines (FOWTs) has attracted increasing attention in the world as they are not restricted by sea water depth compared with bottom fixed offshore wind turbines (OWTs) mounted on monopiles, tripods and jackets. In analogy to traditional offshore oil and gas platforms, different floating foundation concepts (floater) have been proposed in relation to their working performance and economic benefits, such as the spar type, semi-submersible type, tension leg type and barge type floaters. OWTs are often located near the coast close to the traffic lanes, and exposed to the risk to be collided by visiting ships for construction, operation and maintenance and passing commercial ships. From the safety point of view, it is crucial to assess the dynamic responses and damages of OWTs subjected to ship collisions and to design the structures against such accident loads (Yu et al. 2022).

Dynamic responses and damage of different foundation types of OWTs subjected to ship collisions have been extensively studied by nonlinear finite element analysis (NLFEA), and the effects of impact velocity, ship mass, soil stiffness and wind-wave loads have been mainly discussed in previous studies. For example, Moulas et al. (2017) used ABAQUS software to study the effects of collisions of 4000 ton class vessels with a monopile OWT and a jacket-type OWT. Bela et al. (2017) used LS-DYNA solver to investigate the responses of a monopile OWT to collisions with rigid and deformable ship bows at different impact speeds. For ship collisions with FOWTs, the collision responses and damage of a typical NREL 5MW spar-type FOWT was studied by Echeverry et al. (2019), Zhang and Hu (2022), and Ren et al. (2022) using in-house codes or commercial finite element (FE) softwares, in which the effects of impact velocity and wind loads can be found in their studies. Yu et al. (2022) investigated dynamic responses of a 10 MW semi-submersible FOWT mounted on OO-STAR floater under the collisions from ships of 7500 and 150000 tons in terms of parked and operative conditions using NLFEA. A detailed review of research related to ship-OWT collisions can be found in the publication by Ladeira et al. (2022).

Steel circular section tubes are important structural members that are widely used in OWTs and other civil and offshore structures because of their architectural and mechanical advantages. Extensive studies of steel tubes under lateral loads have been previously conducted using experiments, numerical simulations and analytical methods, and the results can be found in the literature. A series of experiments on thin-walled circular tubes under mid-span transverse loading were reported in Refs. (Thomas, 1976) and the deformation modes were identified for the tubes with simply supported boundary conditions.

Søreide and Amdahl (1982) studied the deformation characteristics of both horizontally free and fully axially constrained tubular members under impact loads and demonstrated that the membrane force could increase structural energy absorption. Soares and Søreide (1983) conducted a plastic analysis of a laterally loaded circular tube with various boundary conditions and presented a rigid-plastic analytical formulation for ultimate load analysis. Jones and Shen (1992) investigated the failure mechanism of a fully clamped pipeline impacted by a rigid wedge-shaped indenter at different impact positions. Based on their experiments, a theoretical rigid-plastic method was developed to predict the response of pipes. Wierzbicki and Suh (1988) used theoretical analysis to study axially preloaded circular steel tubes subjected to transverse impact. They found that axial tension can enhance the bending resistance and lateral collapse capacity of tubes, while axial compression significantly reduces the collapse capacity. Yu and Amdahl (2018) conducted a comprehensive review of research on offshore tubular structures against ship collisions, which provides a good understanding of the impact responses of structures and assessment procedures.

From the literature review, it is found that existing research works generally focus on the long slender tubes impacted by a wide indenter. For OWT applications with large diameter tubes, ship collision loads become more concentrated, and the cross-section deformation mechanisms under such concentrated loading are still not clear.

This paper investigated the performance of large diameter steel tubes scaled from the NREL 5 MW spar-type FOWT against concentrated lateral impact loads with a small indenter. An equivalent single-degree-of-freedom (SDOF) model for rigid body motions of FOWT against collision loads was proposed to account for the global motions of the impacted steel tubes. New impact equipment and a steel tube with a scale of 1:30 were designed to meet the experimental requirements. The corresponding finite element modes were established to reproduce the experiments in LS-DYNA. The experimental and simulation results are finally discussed with respected to the deformation behaviors of the steel tubes under lateral impact loads and compared with the analytical models.

2 A SDOF MODEL FOR RIGID BODY MOTIONS OF FOWT SUBJECTED TO COLLISION LOADS

In this study, the well-documented NREL 5 MW spar-type FOWT (Jonkman, 2010) was selected for ship collision analysis and its main dimensions are described in Table 1.

By neglecting the influence of structural flexibilities, rigid body motions of the NREL 5 MW spar-type FOWT can simplified as a 2-DOF model as shown in Figure 1 including the surge motion, q_1, and the pitch motion, q_2, respectively. This model are described in a fixed global coordinate system $OX_1X_2X_3$ with its origin fixed at the center of gravity (COG) of the undeformed system. COB in Figure 1 is the center of buoyancy. According to the results of Refs. (Zhang Z and Høeg C ,2021; Ren et al., 2022; Meng et al. 2022), the equation of motion for the 2-DOF model is given as follows:

$$(\boldsymbol{M}_r+\boldsymbol{M}_{ha})\ddot{\boldsymbol{X}} + (\boldsymbol{G} + \boldsymbol{C}_{aero} + \boldsymbol{C}_{rad} + \boldsymbol{C}_{vis})\dot{\boldsymbol{X}}$$

$$+(\boldsymbol{K}_{buoy} + \boldsymbol{K}_{moor})\boldsymbol{X} = \boldsymbol{F}_C(t) \qquad (1)$$

where $\boldsymbol{M}_r$ is the structural mass matrix, $\boldsymbol{M}_{ha}$ is the hydrodynamic added mass matrix, $\boldsymbol{G}$ is the gyroscopic matrix, $\boldsymbol{C}_{aero}$ is the aerodynamic damping matrix, $\boldsymbol{C}_{rad}$ is the radiation damping matrix, $\boldsymbol{C}_{vis}$ is the viscous damping matrix, $\boldsymbol{K}_{buoy}$ is the restoring matrix, $\boldsymbol{K}_{moor}$ is the linear stiffness matrix of mooring system, and $\boldsymbol{X} = [q_1,q_2]^{\mathrm{T}}$ is the two-dimensional DOF vector. $\boldsymbol{F}_C$ is the contact force vector.

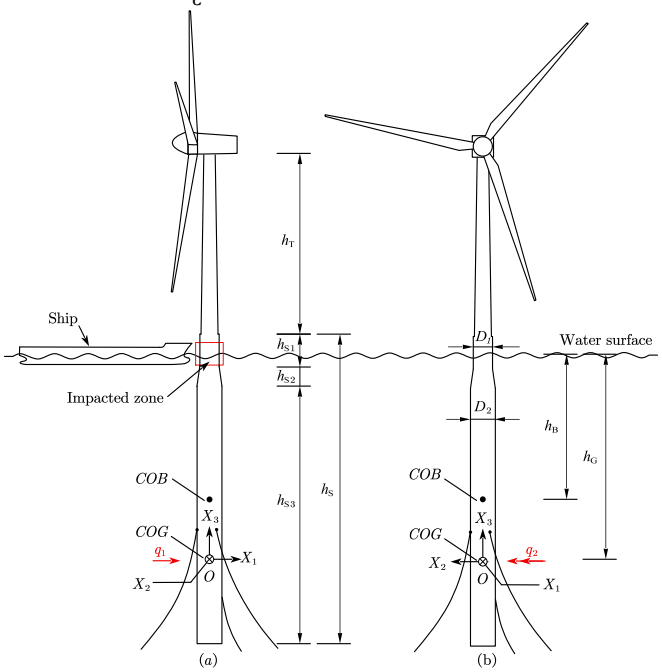

Figure 1. 2-DOF rigid model of spar-type FOWT.

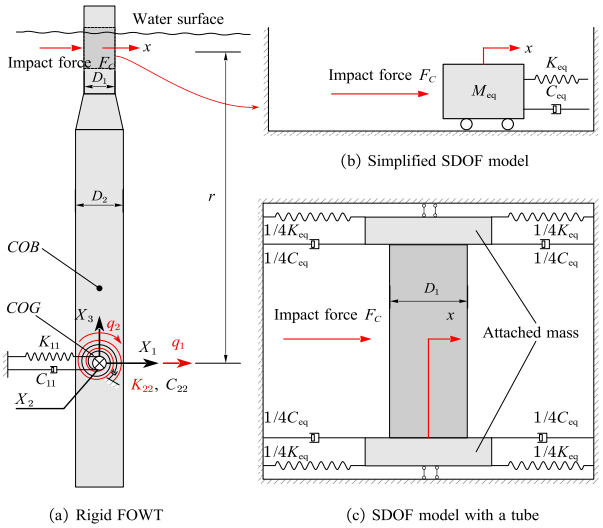

Figure 2. Equivalent SDOF model with a steel tube.

Table 1 Parameters of the 5 MW FOWT (Jonkman, 2010)

Parameter	Value
Tower height, h_T	77.6 m
Spar height above taper top, h_{S1}	14 m
Spar taper height, h_{S2}	8 m
Spar height below taper bottom, h_{S3}	108 m
Spar draft, h_S	130 m
Diameter of spar above taper, D_1	6.5 m
Diameter of spar below taper, D_1	9.4 m
FOWT's COG below SWL, h_G	78 m
FOWT's COB below SWL, h_B	62 m
FOWT's mass, M_{r11}	8.066×10^6 kg
FOWT's inertia in pitch, M_{r11}	1.895×10^{10} kg·m^2
Height from spar bottom to SWL	120 m

The experiment aims to investigate the local deformation of the spar-type FOWT considering the motions of this wind turbine at the impacted region referring to Figure 2 (a). In order to fulfill that, the 2-DOF rigid body motion model shrinks into a SDOF with an equivalent mass, damping and stiffness as shown in Figure 2 (b) and (c). The detailed derivation process of the SDOF model can be found in the recent work by the authors (Ren et al. 2023). The equivalent mass and stiffness in this study are 4.74×10^6 kg and 35032 N/m, respectively. The damping is equal to 5~10% of critical damping that can be calculated by using the mass and stiffness of the SDOF model.

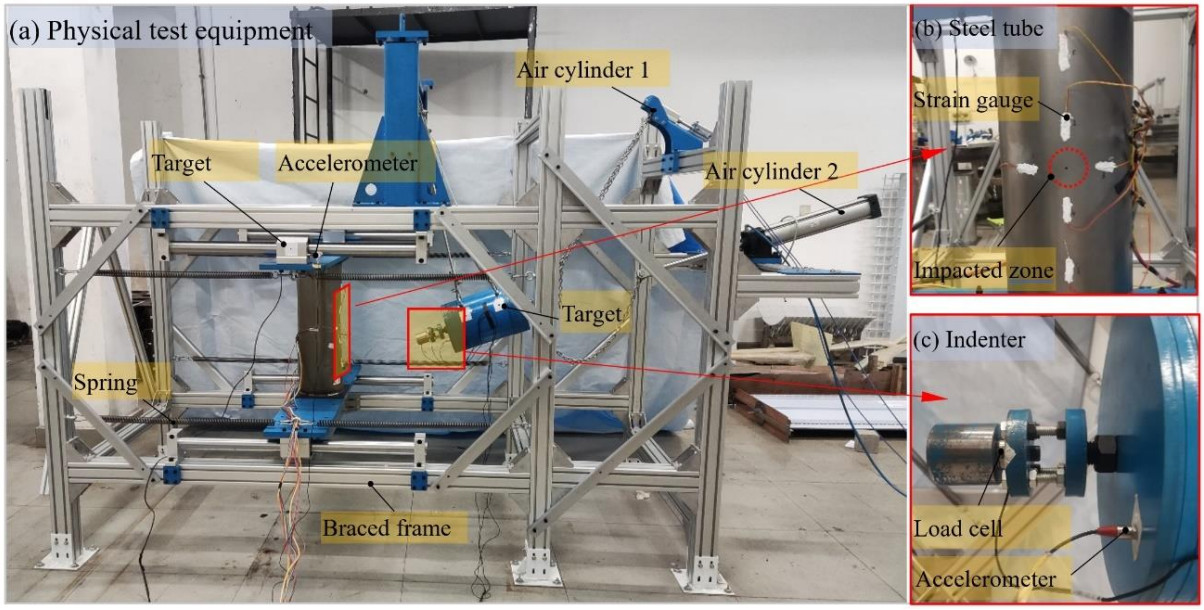

Figure 3. Physical test equipment and instruments.

3 EXPERIMENTAL SETUP

3.1 *Experimental equipment and test instruments*

To examine the deformation behaviors of large diameter steel tubes from a spar-type FOWT subjected to lateral impact loads, new experimental equipment was designed as shown in Figure 3. Test specimens of the scaled steel tubes with welded flanges (240 mm ×240 mm×6 mm) at the two ends were connected to end plates by bolts such that they could slide along the guide rails during and after impact. The mass and the boundary spring stiffnesses can be adjusted according to the SDOF model. The damping in the experimental SDOF system originates from the friction between the sliders and the guide rails. The mass and the maximum velocity of the single pendulum were 101 kg and 3m/s, respectively. The single pendulum was released by air cylinder 1 to obtain the kinetic energy and then pulled back by air cylinder 2 after first collision with the steel tubes to avoid second collision. Both diameter and length of the indenter mounted on the single pendulum were 50 mm. Table 2 shows the parameters of end plates and guide rails.

An accelerometer was mounted on a slider to measure acceleration of the sliding component, as shown in Figure 3 (a), and another accelerometer was mounted on the pendulum to measure its acceleration, as shown in Figure 3 (c). A piezoelectric force transducer (load cell) to measure the impact force was installed between the indenter and the pendulum, as shown in Figure 3 (c). To monitor the strain, eight strain gauges were attached onto the outer surface of steel tube, as shown in Figure 3 (a) and (b). A high-speed video camera was used to measure motions of the sliding component and the single pendulum at a speed of 1600 frames per second.

Table 2. Parameters of end plates and guide rails

Parameter	Value
End plate length	1220 mm
End plate width	240 mm
End plate thickness	20 mm
Guide rail length	1000 mm
Guide rail diameter	50 mm

Table 3. Values of prototype and model.

Parameter	Value	
	Prototype	Model
SDOF model Mass, M_{eq}	4.735×10⁶ kg	175.37 kg (182.55 kg)
Spring stiffness, K_{eq}	35032 N/m	1167 N/m (1960 N/m)
Tube length	18 m	600 mm
Tube diameter	6.5 m	210 mm (200 mm)
Tube thickness	40 mm	1.33 mm (1.2 mm)

Note: The values in brackets were used in the experiments.

3.2 *Experiment design and manufacture*

Considering the experimental conditions and prototype dimensions, a geometric scale of $\lambda = 1:30$ was adopted in the present work. As a preliminary study, a steel tube with a diameter of 6.5 m, length of 18 m and thickness of 40 mm was scaled to conduct impact tests, and the impact point is 4 m below the SWL, namely, r =74 m. The FOWT's mass and stiffnesses were first converted to the SDOF model mass and stiffness to then scale. The detailed values of prototype and model can be found in Table 3.

The steel tubes in the experiment were made of Q345 steel (the yield stress is 345 MPa), which were manufactured by cold rolling of steel plates and welding. The impact scenarios in the experiments were summarized in Table 4.

3.3 *Material properties*

In order to obtain the strain-stress curves of the test tubes, three groups of flat dog-bone specimens were prepared according to the test method of specified in GB/T 228.1-2010 for uniaxial tensile tests. The material used were cut from the same parent steel plate as for the tube specimens. Figure 4 shows the resulting stress-strain relationships from the uniaxial tensile tests in terms of different thickness (1.2 mm ,1.5 mm and 2.0 mm).

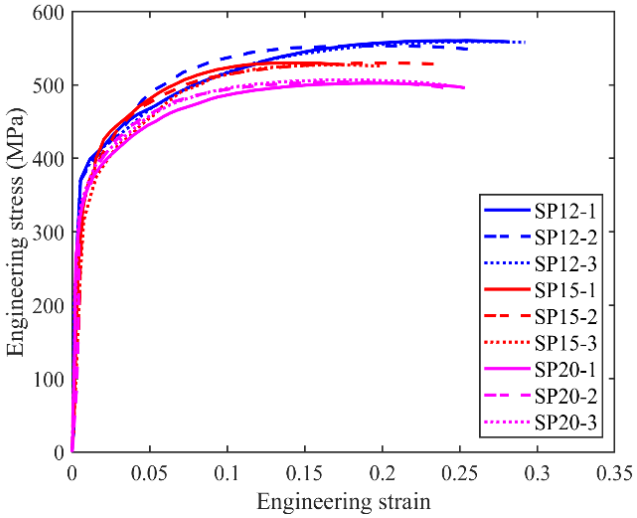

Figure 4. Engineering stress-strain curve of Q345 steel.

Table 4. Steel tube specimen design.

Cases	Total mass (kg)	Steel tube's mass (kg)	Added mass (kg)	Impact velocity (m/s)	Diameter (mm)	Wall thickness (mm)
CS01	182.55	3.48	179.07	**0.89**	200	1.2
CS02	182.55	3.48	179.07	**1.29**	200	1.2
CS03	182.55	3.48	179.07	**1.85**	200	1.2
CS04	182.55	3.48	179.07	**2.35**	200	1.2
CS05	182.55	3.48	179.07	**2.79**	200	1.2

4 NUMERICAL MODELLING

4.1 *Steel tubes, flanges and end plates*

Nonlinear finite element code LS-DYNA was used to reproduce the experiments and the FE models in connection with the experimental cases were established, as shown in Figure 5 (a) and (b). 4-node Belytschko-Tsay shell elements with reduced integration were used for the steel tubes in the numerical models (LSTC, 2018), The mesh size of the steel tubes was 2 mm, as shown in Figure 5 (c). The two end plates and the flanges were simulated by the same element type as the steel tubes. 16 mass elements were attached on the nodes of the end plates, corresponding to the mass blocks in the experiment, as shown in Figure 5 (b).

4.2 *Indenter and pendulum*

The indenter and pendulum were simulated by 8-node solid elements, and the connecting bolts between them were simulated by beam elements which shared common nodes with surrounding solid elements. The mesh size of contact surface of the indenter was 2 mm, as shown in Figure 5 (d).

4.3 *Boundary conditions*

8 spring and damper elements were used to simulate the stiffness and damping. One end of these spring and damper elements shared common nodes with the end plates, while the other end was fully constrained. The stiffnesses were equal to the experimental stiffnesses. The total damping was equal to 45.3 N·s/m, which can be obtained from experimental-free-vibration attenuation curve plotted in Figure 6. The four short edges of the two end plates were fully constrained in the direction of Y and Z but could move freely in the X direction.

4.4 *Material modelling*

The piecewise linear plasticity model (MAT_PIECE-WISE_LINEAR_PLASTICITY) was used to simulate the mechanical behaviors of Q345 steel in which the effective stress–strain curves was obtained from the true stress-strain curve transformed from the experimentally measured engineering stress-strain data. Mild steel is known to be a strain-rate-sensitive material, so that the Cowper-Symonds constitutive was adopted to consider the strain rate effect (LSTC, 2018):

$$\frac{\sigma_d}{\sigma_s} = 1 + \left(\frac{\dot{\varepsilon}}{C}\right)^{\frac{1}{p}} \quad (2)$$

where σ_d and σ_s are the true dynamic yield stress and static stress, respectively.

In this work, two different FE models for the tubes were established for considering the strain rate effects: (1) FE model without strain rate and (2) FE model with strain rate of C=4000 and p=5 (Storheim and Amdahl, 2016). The end plates, flanges, indenter and pendulum were made of Q235 steel with a yield stress of 235 MPa. The density, Young's modulus and Poisson's ratio of the two steels are 7850 kg/m^3, 2.06 ×10^{11} Pa and 0.3, respectively.

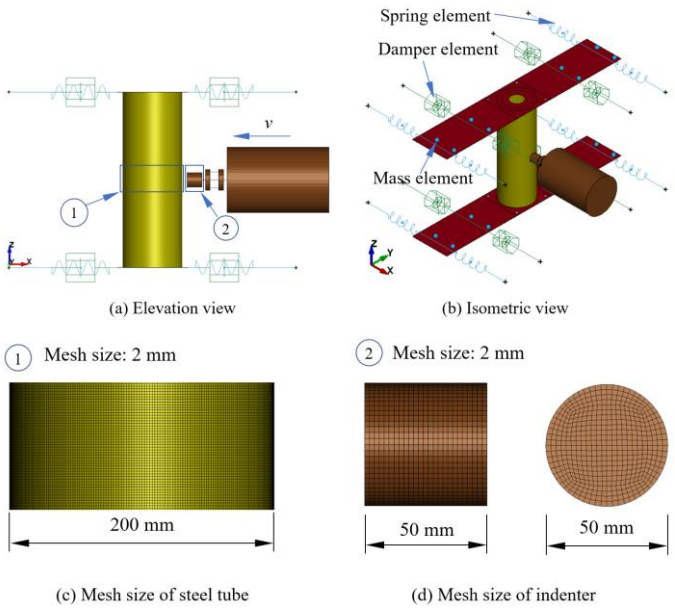

Figure 5. Finite element models of steel tube and pendulum.

4.5 *Comparison of global motions with experiment*

It can be seen from Figure 6 that the free attenuation responses of FE Modelling and test model are in good agreement in general, although there are some differences between the vibration amplitudes due to nonlinear damping in the experiment. The measured model period is 1.9 s which is smaller than the period of 2.438 s scaled from the prototype of the SDOF model with a period of 73.14 s. This is because a greater stiffness was adopted in the test. However, these deviations from damping and stiffness have no influence on the tube local damages, as the forces from damping and stiffness have little contribution on the resistance in a very short impact duration.

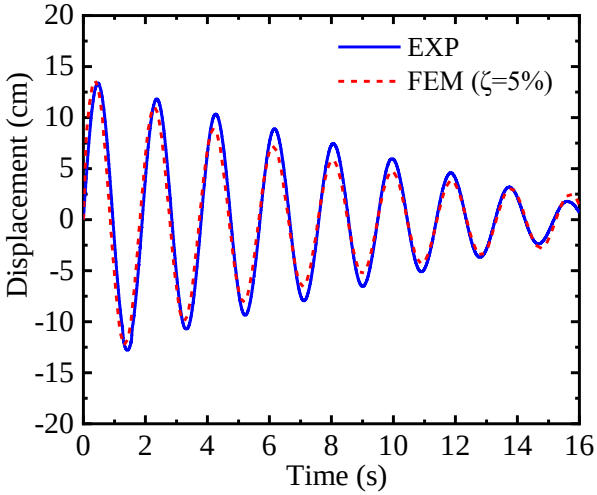

Figure 6. Free decay test of SDOF model

5 RESULTS AND DISCUSSIONS

5.1 *Analysis of experiment and simulation*

Figure 7 shows plots of the typical impact force-time history and impact force-deformation curves from the experiment (EXP) and finite element method (FEM) with various impact energies in the cases of CS01~05 in Table 4. Numerical simulation curves with and without the strain rate effects are presented. The experimental and numerical curves show generally reasonable agreement in the initial stage but tend to deviate after some time, and the experiments yielded smaller peak forces than the numerical results. Figure 7 (b) shows that the slopes of the force-deformation curves in the tests agreed with the numerical results without strain rate at low impact energy, but not well at high impact energy. However, when the strain rate effects with C=4000 and p=5 were considered, the differences in the slopes decreased at high impact energy. The results in Figure 8 showed that the impact force-deformation curves could be divided into three phases which reveal the deformable process of the tubes: (I) initial collapse, where local dents that resemble the shape of the indenter formed on the tubes, and the slopes of force-deformation curves in the tests were steep and agreed well with the numerical modelling results. (II) damage extension stage, in which the damage on the tubes continuously extended in the longitudinal and circumferential directions, and the slopes between the tests and numerical models displayed some evident discrepancies if the strain rate effects were ignored. (III) unloading, where some elastic recoveries of deformations occurred on the tubes prior to completely separate with the indenter.

Figure 9 (a) shows the tube damage for the corresponding cases of CS01~05. Results show that the tube deformation modes were governed by local indentation of the tube cross sections. With low impact velocities, the tube damage resembled the shape of

the indenter with small damage extension along the circumferential and longitudinal directions. As the impact energy increased, the effects of the indenter shape on the tube damage decreased, and the circumferential and longitudinal damage extension dominated and produced damage in the shape of a diamond. The corresponding numerical simulations are shown in Figure 9 (b) and (c), and they indicate that the simulation results without strain rate and with strain rate of C=4000 and p=5 are similar in local deformation modes. When compared with experiments, the sizes of dents in the numerical models without strain rate were similar to the test results at low impact energies. However, for high impact energies, the sizes of dents in the models considering strain rate effects were more consistent with the test outcomes.

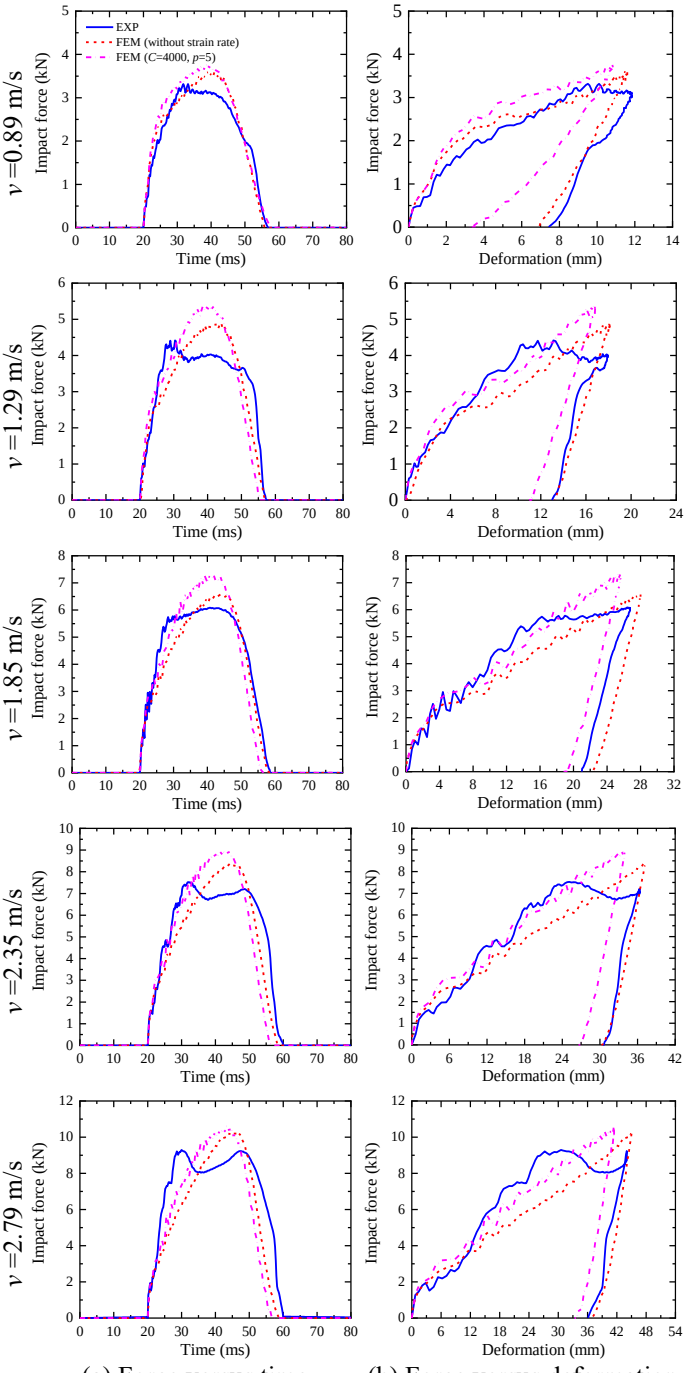

(a) Force versus time (b) Force versus deformation

Figure 7. Impact force-time history and Impact force-deformation curves for different impact velocities.

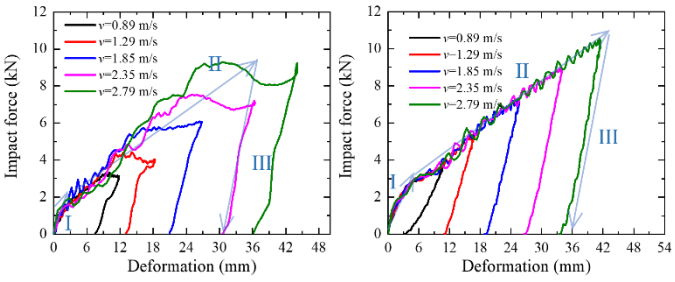

(a) Experiment (b) FEM (C=4000, p=5)

Figure 8. Force versus deformation curves for different impact velocities.

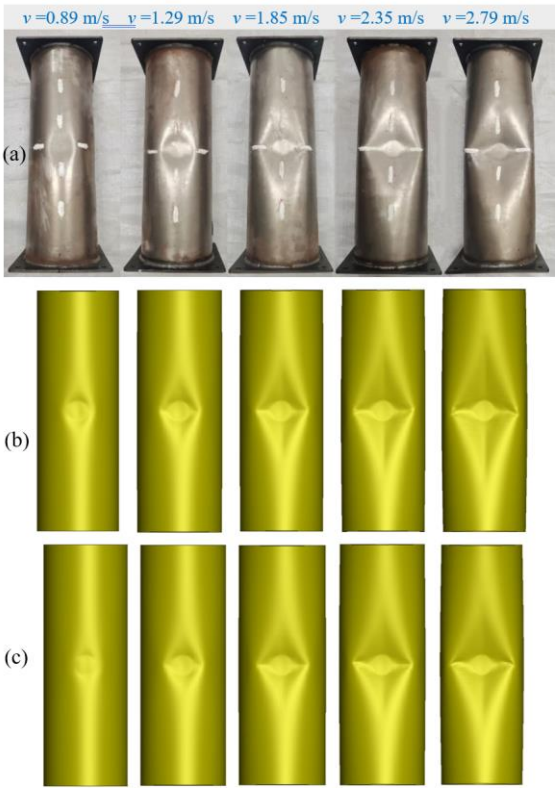

Figure 9. Deformation modes of steel tubes under different impact velocities: (a) experiment, (b) FEM (without strain rate) and (c) FEM (C=4000 and p=5)

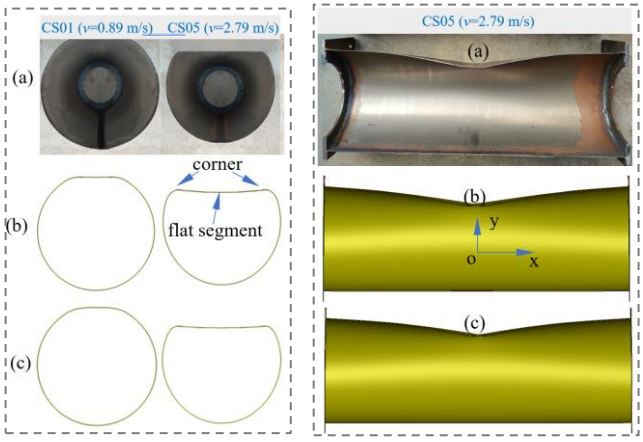

Figure 10. Cross and longitudinal sections of tubes: (a) experiment, (b) FEM (without strain rate), (c) FEM (C=4000 and p=5).

The cross and longitudinal sections of the tubes (CS01and CS05) after impacts are shown in Figure 10. Interestingly, top segments of the damaged tubes from the experiments were almost flat. Numerical

simulation results, however, showed slightly higher shoulders at the two corners of the deformed tube cross sections than at the middle of the tubes. The differences were very small, though. The longitudinal deflections in the numerical models extended to the tube ends even when the strain rate effects were considered. However, in the experiments, no visible deflections were observed near the tube ends.

5.2 *Comparison with conventional theoretical models*

Theoretical models are useful tools for quick and reliable assessments of structural responses under accidental loads and are also widely used in design rules and standards (e.g., DNV RP C204). A few analytical models are available in the literature for the indentation resistance of slender tubes subjected to the impact by wide indenters.

Amdahl (1980) proposed a local denting model based on a plastic yield line analysis, and the model related the denting resistance to local indentation. This model used a flat indenter and considered the contact width effect. The model is adopted in NORSOK N-004 (2004), and the form of the denting resistance is as follows:

$$\frac{R}{R_c} = \left(22 + 1.2\frac{B}{D}\right)\left(\frac{w_d}{D}\right)^{\frac{1.925}{3.5+\frac{B}{D}}}\sqrt{\frac{4}{3}\left[1-\frac{1}{4}\left(1-\frac{N}{N_P}\right)^3\right]} \qquad (3)$$

where B is the contact width of the indenter, D is the tube diameter, w_d is the dent depth, N is the axial load, and N_P is the plastic yield resistance. The last term was borrowed from Wierzbicki and Suh (1988) to account for the effect of axial functional loads in the leg. R_c is a characteristic resistance of the tube and is defined as:

$$R_c = \sigma_y \frac{t^2}{4}\sqrt{\frac{D}{t}} \qquad (4)$$

Wierzbicki and Suh (1988) first derived a closed form solution for the indentation resistance of tubes under combined loading in the form of lateral indentation, bending moment and axial force. The problem was decoupled into the bending and stretching of a series of unconnected rings and generators. The indentation resistance is given as:

$$R = 16\sqrt{\frac{2\pi}{3}\frac{D}{t}\frac{w_d}{D}\frac{1}{4}\sigma_y 4t^2}\sqrt{\left[1-\frac{1}{4}\left(1-\frac{N}{N_P}\right)^3\right]} \qquad (5)$$

Figure 11 shows the comparison of indentation resistances in terms of experiments, numerical simulations and theoretical models. It is found that the theoretical models predict much larger resistance (almost doubled) than the experimental and numerical results, which is very unconservative. The reason is that the analytical models based on the investigation of tubes impacted by an indenter whose width is larger than the tube diameter. Therefore, the large contact loading rather than the concentrated in previous experiments, which leads to different cross section deformation patterns and thereby resistances.

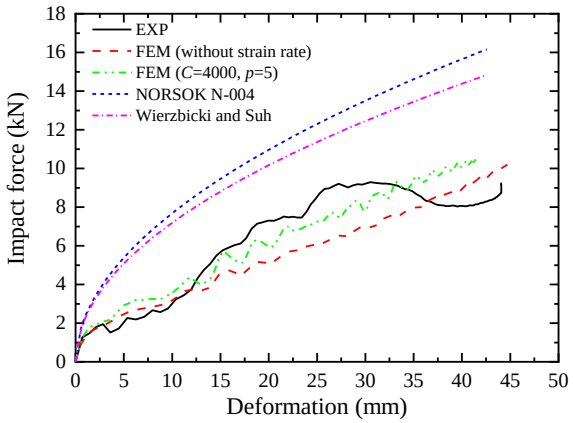

Figure 11. Comparison of indentation resistances.

6 CONCLUSIONS

This paper investigates the deformation behaviors of large diameter steel tubes from a FOWT under concentrated lateral impact loads using experiments and numerical simulations. Results show that deformation of large diameter tubes could generally be divided in three phases: (I) initial collapse, (II) damage extension stage and (III) elastic unloading with deformation recovery. The deformation modes of large diameter tubes were governed by the local indentations of tube cross sections. The dented shapes progressively developed to resemble a diamond with increasing impact energy. Numerical simulations with strain rate effects reasonably reproduced the force-deformation curves from experiments. By neglecting strain rate effects, the simulation results became conservative. Existing models for indentation resistance overestimated the bearing capacity of large diameter tubes. This indicated needs for new analytical models for indentation resistance of large diameter tubes.

ACKNOWLEDGMENTS:

This research was supported by the Intergovernmental International Innovation Cooperation of China National Key Research and Development Plan (Grant Number: 2016YFE0127900) and Research Council of Norway via the Centers of Excellence funding scheme (Project Number: 223254 – NTNU AMOS).

REFERENCES

Amdahl J. 1980. Impact Capacity of Steel Platforms and Tests on Large Deformations of Tubes and Transverse Loading. Det norske Veritas. *Progress Report* (10), 80–0036.

Bela A, Le Sourne H, Buldgen L, Rigo P. 2017. Ship collision analysis on offshore wind turbine monopile foundations. *Marine Structures* 51: 220-241.

Echeverry S, Marquez L, Rigo P, Le Sourne H. 2019. Numerical crashworthiness analysis of a spar floating offshore wind turbine impacted by a ship. *Proceedings of the 8th international conference on collision and grounding of ships and offshore structures (ICCGS 2019)*, October 2019. Lisbon, Portugal: CRC Press.

GB/T 228.1-2010. Metallic Materials-Tensile Testing-Part 1: Method of Test At Room Temperature, *Standards Press of China*.

Jonkman, J. 2010. Definition of the Floating System for Phase IV of OC3. *National Renewable Energy Laboratory*, Golden, Colorado.

Jones N, Shen WQ. 1992. A theoretical study of the lateral impact of fully clamped pipelines. *Proc Inst Mech Eng Part E-Journal of Process Mechanical Engineering* 206(2): 129-146.

Ladeira I, Márquez L, Echeverry S, Le Sourne H, Rigo P. 2022. Review of methods to assess the structural response of offshore wind turbines subjected to ship impacts. *Ships and Offshore Structures*, 1-20.

LSTC, LS-DYNA keyword user's manual. 2018. *Livermore Software Technology Corporation*.

Moulas D, Shafiee M, Mehmanparast A. 2017. Damage analysis of ship collisions with offshore wind turbine foundations. *Ocean Engineering* 143: 149-162.

Meng Q, Hua X, Chen C, Zhou S, Liu F, Chen Z. 2022. Analytical study on the aerodynamic and hydrodynamic damping of the platform in an operating spar-type floating offshore wind turbine. *Renewable Energy* 198: 772-788.

NORSOK Standard N004. 2004. Design of Steel Structures, Appendix a, Design against Accidental Actions. *Det Norske Veritas*.

Ren Y, Meng Q, Chen C, Hua X, Zhang Z, Chen Z. 2022. Dynamic behavior and damage analysis of a spar-type floating offshore wind turbine under ship collision. *Engineering Structures* 272: 114815.

Ren Y, Yu Z, Hua X, Amdahl J, Zhang Z, Chen Z. 2023. Experimental and numerical investigation on the deformation behaviors of large diameter steel tubes under concentrated lateral impact loads. *International Journal of Impact Engineering: in review*.

Storheim M, Amdahl J. 2017. On the sensitivity to work hardening and strain-rate effects in nonlinear FEM analysis of ship collisions. *Ships and Offshore Structures* 12(1): 100-115.

Søreide TH, Amdahl J. 1982. Deformation characteristics of tubular members with reference to impact loads from collision and dropped objects. *Norwegian Maritime Research Paper 2, Norwegian Maritime*, 3-12.

Soares CG, Søreide TH. 1983. Plastic analysis of laterally loaded circular tubes. *Journal of Structural Engineering* 109(2): 451-467

Thomas SG, Reid SR, Johnson W. 1976; Large deformations of thin-walled circular tubes under transverse loading—I: an experimental survey of the bending of simply supported tubes under a central load. *International Journal of Mechanical Sciences*18(6): 325-333.

Wierzbicki T, Suh MS. 1988, Indentation of tubes under combined loading. *International Journal of Mechanical Sciences* 30(3-4): 229-248.

Yu Z, Amdahl J, Rypestøl M, Cheng Z. 2022. Numerical modelling and dynamic response analysis of a 10 MW semi-submersible floating offshore wind turbine subjected to ship collision loads. *Renewable Energy* 184: 677-699.

Yu Z, Amdahl J. 2018. A review of structural responses and design of offshore tubular structures subjected to ship impacts. *Ocean Engineering* 154: 177-203.

Zhang Y, Hu Z. 2022. An aero-hydro coupled method for investigating ship collision against a floating offshore wind turbine. *Marine Structures* 83: 103177.

Zhang Z, Høeg C. 2021. Inerter-enhanced tuned mass damper for vibration damping of floating offshore wind turbines. *Ocean Engineering* 223: 108663.